FULL RESEARCH ARTICLE

Fatigue response of AlSi10Mg by laser powder bed fusion: influence of build orientation, heat, and surface treatments

S. Fini[1] · D. Croccolo[1] · M. De Agostinis[1] · G. Olmi[1] · L. Paiardini[1] · C. Scapecchi[1] · M. Mele[1]

Abstract

The aim of this study is to analyze how the fatigue behavior of AlSi10Mg by laser powder bed fusion is affected by build orientation, heat, and surface treatments. A three-by-three factorial plan has been arranged for this purpose. Particularly, regarding the heat treatment, three levels were considered (as built, age hardening, and stress relief); whereas, for the surface treatment, three levels were investigated (micro-shot-peening, micro-shot-peening plus fine blasting, and machining and lapping following laser powder bed fusion). Regarding the build orientation, the specimens were manufactured using three different build orientations (0°, 45°, and 90°). The obtained data have been statistically analyzed by a three-factor ANOVA-based method. The results, supported by fractographic and micrographic microscopy analyses, indicate that the age-hardening treatment yields the maximum benefits, whereas stress relief may even have a detrimental effect. As for surface treatments, a positive influence of shot-peening has been found.

Abbreviations

AM	Additive manufacturing
ANOVA	Analysis of variance
b_0, b_1	S–N curve coefficients according to standard
DMLS	Direct metal laser sintering
LPBF	Laser powder bed fusion
N	Lifecycles (for S–N curve)
PBF	Powder bed fusion
PBO	Part build orientation
R	Stress ratio (fatigue tests)
Ra	Roughness average (μm)
SLM	Selective laser melting
S	Maximum bending stress (for S–N curve), corresponding also to the stress amplitude.
SSBR	Sum of squares between rows (for ANOVA computations)
SSBC	Sum of squares between columns (for ANOVA computations)
SSBP	Sum of squares between profundities (for ANOVA computations)
SSI	Sum of squares interaction (for ANOVA computations)
SSE	Sum of squares error (for ANOVA computations)
$\bar{S}$	Overall mean (for ANOVA computations)
S–N	Fatigue curve in the finite life domain

✉ C. Scapecchi
   chiara.scapecchi@unibo.it

1   Department of Industrial Engineering (DIN), University
    of Bologna, Viale del Risorgimento 2, 40136 Bologna, Italy

1 Introduction

Modern additive manufacturing (AM) processes enable the fabrication of metal parts with very complex geometries, which are often difficult to obtain (as a monolithic component) by machining or through conventional subtractive processes. It is also possible to optimize the component design for lightness purposes, obtaining parts with high strength/weight or stiffness/weight ratios. Furthermore, additive processes are often faster than conventional ones (and sometimes even cheaper) when manufacturing a small number of components [1]. The raising interest in additive manufacturing is helping with the advancement of numerous numerical and artificial intelligence based tools tailored to enhance the quality of AM components [2, 3].The most applied additive manufacturing processes for metal parts are based on powder bed fusion (PBF). Specifically, laser powder bed

fusion (LPBF) covers the overwhelming majority of applications [4–6]. In this process, the 3D model of the part is first sliced in layers. At the beginning of the process, a recoater deposits a layer of powder on a building plate. Then, a laser driven by galvo-mirrors selectively fuses the cross section of the first layer. Once scanning is completed, the build plate moves downward by the height of the molten layer. Then, a further powder layer is spread again over the previous one, and the next section is transformed. These steps are repeated until part completion [7–11]. At the end of the process, the unmelted powder is removed and the parts are cut from the build plate by means of Electrical Discharge Machining (EDM) or bandsaw [12].

Static and dynamic mechanical properties of components made in AM are often different from those of parts made of wrought material. This outcome arises from AM processes being often affected by defects, such as porosity, internal voids, and oxides, as well as poor surface finishing. Furthermore, the heterogeneous temperature variations components undergo during fabrication are likely to trigger residual stresses due to very high material melting and cooling rates. The high energy concentration of the laser spot results in the rapid melting of the material and the formation of a Heat Affected Zone (HAZ) in the surrounding regions. Heat exchange with the unmelted powder and the environment contributes to the rapid cooling of the molten material to the bed temperature, as demonstrated by [13]. The high thermal gradient usually results high residual stresses [14]. Another important issue concerns surface finishing: in fact, components made by LPBF exhibit a very high surface roughness (even more than $Ra = 20 \, \mu m$). These features were found to detrimentally affect the fatigue response for many materials, namely AlSi10Mg aluminum alloy [15–17], TiAl6V4 titanium alloy [18], maraging steel [19, 20], 316L stainless steel [21] and nickel based alloy 718 [22]. Heat and surface treatments are expected to improve the performance as an effect of microstructure enhancement [23, 24], residual stress drop, or surface roughness decrease. Machining may improve surface finishing, also removing the surface layer, in particular surface contours, where defects are generally more concentrated [25]. A further factor that is likely to affect the performance of additively processed parts is post-process surface treatment. Particularly, shot-peening is a widely used surface treatment that generally has a positive effect against fatigue and can be applied to several materials, including stainless steel and metal alloys [26]. Its main capabilities include the reduction of porosity and the generation of a beneficial compressive residual stress state at the surface and just beneath it. Previous studies on additively manufactured Ti6Al4V have highlighted fatigue strength enhancement [27] in pre-heat-treated samples that have been fatigued under four-point rotary bending. The fatigue response improvement arises from the induced negative residual stresses that have the capability of retarding both surface crack initiation and propagation [28–30]. This mechanism relies on cracks needing greater cyclic stress levels to grow up to final breakage, even though the surface is made more irregular than in the ground state. In addition, the scatter affecting fatigue strength and S–N curves is also reduced [31]. However, sometimes, surface damage due to the treatment may promote the initiation of a few surface cracks. The beneficial impact of shot-peening is also highlighted in O'Brien JM et al. [32], where a numerical analysis involving an additively processed stainless steel has been run. Their results indicate that heat treatment and shot-peening have the capability of relaxing the stacking process-induced tensile residual stresses and, in addition, generating a significantly compressed layer at the surface. Some authors have also observed an effect of grain refinement [33, 34]. Process parameters, such as Part Build Orientation (PBO), are also important, as highlighted in Todai [35]. Both the overall number of layers needed to manufacture a part and the time for scanning a layer are highly dependent on part orientation on the build platform [15, 36]. For example, when fabricating a cylindrical sample lying on the plate, a reduced number of layers is needed, but laser scans of each section are remarkably long and take a longer time with respect to a vertically oriented specimen. Moreover, due to the widely extended layer in the first case, it may be hard to maintain the perfect perpendicularity between the laser direction and the impacted surface, which may deteriorate material properties. The number of simultaneously manufactured components on the build platform is also likely to affect the final microstructure. The higher the number of components to be fabricated together, the higher the elapsed time between two subsequent depositions of powder layers. Consequently, a different thermal cycle may be induced, which is likely to result in different microstructures and, as a consequence, mechanical properties.

Among the most widespread alloys for AM processes, AlSi10Mg is of particular interest in the industrial field. In fact, it is widely used to manufacture lightweight parts (such as frames, motorbike swingarms, and pistons) with good mechanical performance. Its weldability makes it suitable for additive processes and for thin component fabrication. Many studies are available in the literature [37–39] regarding the static properties of the aforementioned alloy. In addition, further data are often provided by powder supplier datasheets. On the other hand, very few studies have been dedicated to additively manufactured AlSi10Mg fatigue properties [40, 41]. Therefore, the present study focused on the fatigue behavior of this alloy. The static properties of AlSi10Mg provided by the powder supplier (EOS GmbH [42]) for machined samples without heat treatment for both vertically and horizontally oriented specimens exhibit relevant differences. In
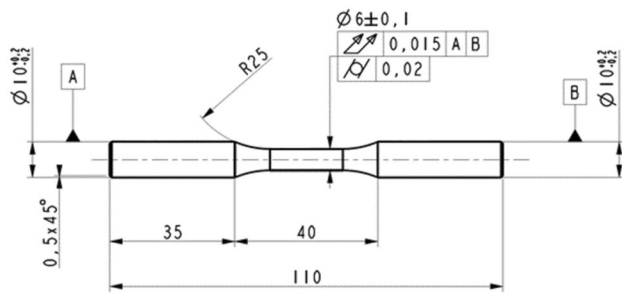
Fig. 1 Sample geometry specification, inspired by ISO 1143

fact, additively manufactured parts are generally sensitive to the build orientation, especially if no heat treatment is performed after the process. In this case, the observed microstructure is not homogeneous, as it is affected by the heating transfer and, consequently, in turn, by the build orientation. Therefore, heat treatment has a relevant role in strengthening the microstructure or making it more uniform among the available post-manufacture treatments. A frequently recommended one for this specific Al alloy is the T6 heat treatment [43, 44], consisting of solution annealing, quenching, and subsequent artificial aging. The solution annealing is conducted to dissolve soluble phases containing Mg or other trace elements, homogenize the composition, and spheroidize the Si phase, whereas quenching maintains the solution phase that formed at high temperature, while bringing the material to low temperature (generally room temperature). After aging, a uniform distribution of precipitates that strengthen the treated material can be achieved. Another possible heat treatment for aluminum alloys is stress relief (SR). In general, the differences in microstructure, as well as the differences in achievable mechanical properties for different build orientations in as-built samples can be potentially reduced by stress relief [45, 46]. Therefore, this paper aims to assess the fatigue properties of additive manufactured AlSi10Mg and study the influence of build orientation,

heat and surface treatments on fatigue. The study is also completed by (stereoscopic, optical, scanning electron) microscopy analyses for result interpretation.

2 Materials and methods

2.1 Design of experiment and manufacturing of samples

The specimens were designed with a smooth cylindrical geometry according to Standard ISO 1143 [47] for rotating bending fatigue testing, as indicated in Fig. 1.Due to production costs, the minimum diameter recommended by the Standard was chosen. The powder was supplied by EOS GmbH. The given chemical composition is listed in.

Table 1, whereas the given particle size distribution is 25–70 μm. All the specimens were manufactured by EOSINT M290 device equipped with Ytterbium fiber laser with 400W power, with working space 250 mm wide and 250 mm long. The layer thickness was 30 μm, the volume rate was 5.1 mm³/s, and the build platform temperature was 35 °C, as suggested by EOS GmbH [42]. A nominal hatch distance of 160 μm was set, following suggestions found in literature [41, 48]. All the samples have been manufactured by an external supplier.

The experimental design for the fatigue campaign involved three factors: build orientation, heat treatment, and surface treatment. Each factor was considered over three levels, as reported in Table 2. A five-character alphanumeric code was used as specimen ID (e.g., ADG01). The coding reference is reported in Fig. 2.

The three levels for the build orientation consisted of 0° (horizontally built samples, Axx sets, with supports), 45° (slanted samples, Bxx sets, with supports just under the grip areas), and 90° (vertically built samples, Cxx sets, without supports). Regarding the heat treatment, the studied levels were untreated (xDx sets), processed by T6 (xEx sets), and by stress relief (xFx sets). These two treatments were

Table 1 AlSi10Mg chemical composition (wt%) [42]

Al (%)	Si (%)	Fe (%)	Cu (%)	Mn (%)	Mg (%)	Ni (%)	Zn (%)	Pb (%)	Sn (%)	Ti (%)
87.5–90	9–11	≤0.55	≤0.05	≤0.45	0.25–0.45	≤0.05	≤0.1	≤0.05	≤0.05	≤0.15

Table 2 AlSi10Mg fatigue experimental plan

		Levels		
Factors	Build orientation	0° (A)	45° (B)	90° (C)
	Heat treatment	No H.T. (D)	T6 (E)	Stress relief (F)
	Surface treatment	Micro-shot-peening. (G)	Micro-shot-peening + fine blasting(H)	Machining + Lapping (I)

Fig. 2 Coding system for the fatigue samples
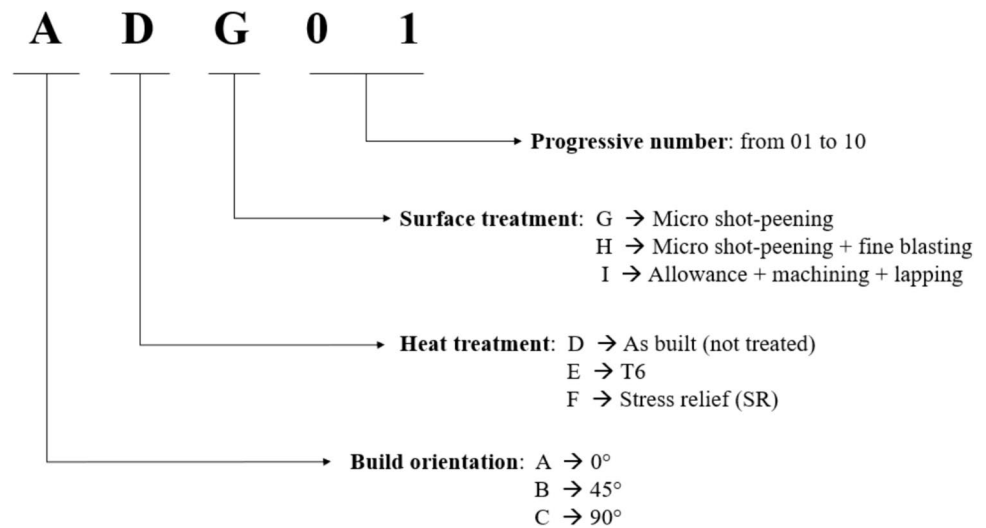
performed after fabrication. T6 age hardening (xEx sets) entailed initial heating up to 520 °C; this temperature was kept constant for one hour. Afterward, water quenching was performed (water at 25 °C). Eventually, the samples were heated again and kept at 160 °C for six hours (as suggested by EOS [42]), and a final water quenching was performed. More in-depth insights into this treatment can be found in [49, 50]. The stress relief treatment (xFx sets) was carried out by heating the specimens at 300 °C for two hours and then gradually cooling them in fresh air. Performing heat treatments indeed entails additional costs affecting the production process. Therefore, the untreated level (xDx) was also considered and taken as a reference to quantify the benefit produced by these treatments and to evaluate their usefulness. As for surface treatments, three different conditions were considered: shot-peened (xxG sets), shot-peened and sand-blasted (xxH sets), and, lastly, machined and lapped (xxI sets). Following machining and lapping, the surface roughness sharply drops down, thus also removing most of the surface and sub-surface defects that often promote crack initiation and propagation. Theoretically, this treatment was expected to increase the fatigue strength. However, it indeed adds costs to the production cycle. Furthermore, complex geometries could be difficult to machine. Thus, a widely used surface treatment, i.e., micro-shot-peening followed by fine blasting, was added to the experiment. The only micro-shot-peening level was set as a benchmark to quantify the improvements arising from the other treatments. Shot-peening was performed by ceramic beads Z300. A 3^3 experimental plan was designed, accounting for 27 sample sets corresponding to each different combination. When both heat and surface treatment were applied, the surface treatment was performed first. A total amount of ten specimens per type (270 samples) was tested. The experimental procedure can be summarized as follows:

1. Diameter and roughness measurements (Ra).
2. Misalignment measurements.
3. Determination of the mechanical properties by static tests.
4. Execution of 4-point rotating bending fatigue tests.
5. Density measurements.
6. Fractographic analyses.
7. Micrographic analyses by field emission gun scanning electron microscope (SEM-FEG).

2.2 Dimensional and surface measurements

Diameter and roughness measurements were performed to check the compliance with design specifications. The dimensional checks were carried out by an electronic micrometer (resolution of 0.001 mm). Six diameter measurements were taken at the gage and four at each head. Roughness measurements were carried out both at the gage and at the heads by a portable surface roughness tester with a resolution of 0.001 μm (RT25, SM Metrology System, Torino, Italy). Roughness measurements were averaged over 4 mm runs along the specimen longitudinal axis at 90° angled spots, considering two replications per spot for a total number of 8 replications. Actual diameter dimensions were used to accurately evaluate the static strengths and to calculate the load to be applied during the fatigue tests. Sample misalignment at gage was checked by a centesimal comparator applied to the 4-point bending machine before every fatigue trial.

2.3 Density measurements

Density measurements were carried out by the immersion method. The procedure consists of two weight measurements: in the first one, the sample's weight in the air ($w_{sample\_in\_air}$) is measured, whereas, in the second one, the

sample's weight, upon complete immersion in distilled water ($w_{sample\_in\_liquid}$) is determined. The difference between these two terms yields the Archimedes force (S_{Archim}).

$$S_{Archim} = w_{sample\_in\_air} - w_{sample\_in\_liquid}. \tag{1}$$

Dividing the Archimedes force by the gravity acceleration and by the liquid density (ρ), which is calculated by the machine as a function of temperature, the specimen's overall volume (V_{sample}) is obtained.

$$V_{sample} = \frac{S_{Archim}}{\rho \cdot g}. \tag{2}$$

The specimen's density (ρ_{sample}) is finally calculated by dividing the specimen mass by its volume.

$$\rho_{sample} = \frac{w_{sample\_in\_air}/g}{V_{sample}}. \tag{3}$$

The density evaluation made it possible to get insights about the internal porosity level because specimens with high porosity levels exhibit a lower density. In additively manufactured components, porosity does not only depend on the used fabrication process parameters but is also affected by the application of post-process heat treatments. In fact, the heat treatment thermal cycles can also increase the dimensions of the pores, causing a decrease in density. The density of all samples was measured with three replications.

2.4 Static testing

Static tensile tests were initially performed involving specimens manufactured along the three different build orientations (0°, 45° and 90°). Five samples per build orientation were manufactured, according to ISO 6892-1 [51] (Fig. 3). Specimens were shot-peened and no heat treatment was

applied in order to get data that could be compared to those by the supplier [42]. For the static tests, a servo-hydraulic testing machine equipped with a 100 kN load cell was used. The heads of the specimens were threaded to be coupled to the machine fixtures. For the elongation measurements, an HBM DD1 Extensometer (with initial length $l_0 = 25$ mm) was used. Tests were carried out in the displacement-controlled mode (1 mm/min) for a stress rate ranging from 7 to 14 MPa/s, in agreement with ISO 6892-1 [51], which recommends a value between 2 and 20 MPa/s for metallic materials with Young's modulus lower than 150 GPa.

2.5 Fatigue testing

For fatigue testing, a four-point rotating bending machine was used (frequency of 60 Hz and stress ratio R = −1). The samples were fatigued until failure or up to 10^6 cycles, with the aim of determining the fatigue curve in the finite life domain (between 10^3 and 10^6 cycles), thus also working out the fatigue strength at 1 million cycles by interpolation. The stress amplitude, corresponding to the maximum bending stress, varied between 200 and 20 MPa.

2.6 Fracture, microstructure, and chemical composition analysis

After the fatigue tests, fracture surfaces were analyzed by a stereographic microscope (Zeiss Stemi 305) to detect the crack initiation point and assess the fracture mode. To determine the fracture behavior, the microstructure and the chemical composition, micrographics, and high magnification images were captured by an optical microscope (Nikon Optiphot 100) and a Tescan Mira 3 SEM-FEG. The main steps that were followed to obtain the micrographies are provided below:

Fig. 3 Tensile tests sample drawing
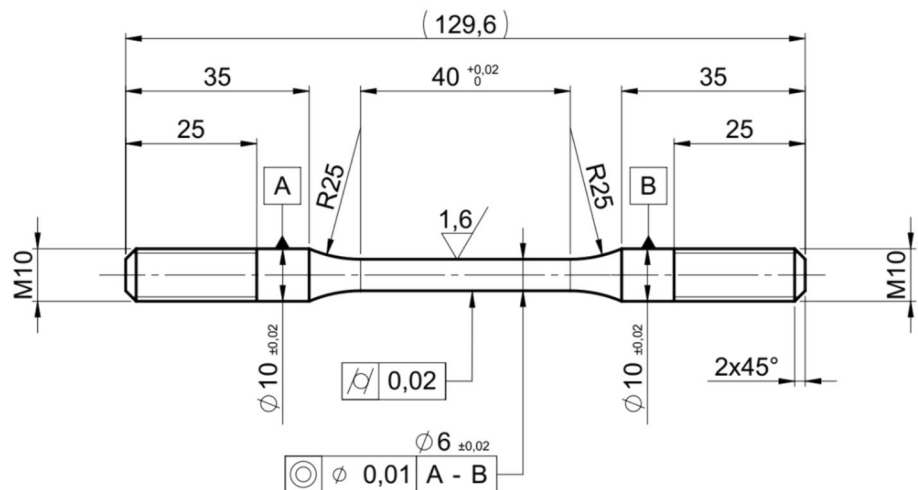
- Two sections of the sample's gage were cut: one parallel and the other one perpendicular with respect to the base plate.
- The cut sections were embedded in a resin. Considering that electrochemical tests were not needed, insulating resin was used.
- Polishing of the resin-incorporated specimens. They were sanded by increasingly fine-grained papers (grain from P60 to P2500) and subsequently polished by cloth disks wetted by alumina powder dissolved in water (0.01 μm grain of alumina powder).
- Surface chemical etching. The chemical reagent used is Keller's reagent. It was applied at room temperature for 27 s. The specimens were then washed with water and dried.

3 Results

3.1 Diameter and roughness results

The mean measured values for gage diameter and gage roughness are reported in Table 3 with reference to the specimens involved in the static tensile tests.

The "AT" group refers to the horizontally built samples, "BT" to the slanted oriented samples, and "CT" to the vertically built samples. As described above, six diameter measurements and eight roughness measurements were carried out per sample. Regarding gage diameters, values differing

by a few hundredths of a mm from the designed value were found. Considering the specimens were in the unmachined state and dimensions were close to the recommended ones, they were considered acceptable, provided that actual dimensions were considered for further processing. As for roughness, related values were found to be consistent with the performed process and the post-process treatments. The roughness exhibits higher values and standard deviations in horizontally built samples rather than in vertically built ones. A worse roughness for horizontal specimens was due to a poor finishing that mainly affects the lower faces (those on the supports). For this set, a mean value of 10.9 μm was calculated, but values up to 22 μm were measured. Nevertheless, for horizontal samples (AT), surface finishing was greater than those in the powder supplier datasheets [42, 52], whereas for the vertically built set (CT), comparable values were obtained.

The same procedure was used to check the gage diameter and roughness of samples used in fatigue tests. Results are listed in Tables 4 and 5.

It is interesting to observe that the standard deviation in the case of micro-shot-peened and sand-blasted (xxH) samples is generally lower than that for only shot-peened ones (xxG), which indicates slightly better dimensional repeatability. Machining indeed improves surface finishing (xxI); however, a slightly higher roughness than expected, which is likely to affect fatigue properties, was found in ADI, BDI, and CDI families. After a polishing treatment, such as that planned for the "xxI" series, the expected roughness is normally in the order of 0.8 μm. No significant differences were observed between shot-peened and fine-blasted samples.

3.2 Static tests results

A representative static test curve relating stress (σ) and strain (ε) is shown in Fig. 4. The noise shown in the plastic part of the graph is due to the PLC-effect.

The experimental results are also collected in the bar graph in Fig. 5. The obtained yield strength ($Rp_{0.2}$) and Young's modulus (E) were consistent with those declared

Table 3 Gage diameters (in mm) and gage roughness (in μm)

	Gage diamenter			Gage roughness	
	Mean value	St. dev.		Mean value	St. dev.
AT	6.041	0.074	AT	10.929	5.186
BT	6.048	0.044	BT	8.387	1.378
CT	5.978	0.018	CT	7.651	0.936

Mean value and standard deviation for sample families used for static tensile tests

Table 4 Gage diameters

|	Mean value	St. dev.		Mean value	St. dev.		Mean value	St. dev.
A D H	5.818	0.061	B D H	6.040	0.060	C D H	5.977	0.016
A D I	6.037	0.052	B D I	6.009	0.007	C D I	6.011	0.004
A E G	5.877	0.146	B E G	6.008	0.038	C E G	5.983	0.027
A E H	5.915	0.111	B E H	6.000	0.036	C E H	5.991	0.022
A E I	6.016	0.006	B E I	5.989	0.006	C E I	6.016	0.005
A F G	6.038	0.096	B F G	6.076	0.074	C F G	5.994	0.025
A F H	6.044	0.075	B F H	6.054	0.056	C F H	5.988	0.021
A F I	6.008	0.004	B F I	5.988	0.009	C F I	6.008	0.006

Mean value and standard deviation for sample families used in fatigue tests (all dimensions in mm)

Table 5 Gage roughness

	Mean value	St. dev.		Mean value	St. dev.		Mean value	St. dev.
A D G	5.668	1.945	B D G	4.964	1.530	C D G	5.569	1.361
A D H	3.772	1.266	B D H	5.152	1.708	C D H	6.113	1.495
A D J	1.217	0.272	B D I	2.722	0.522	C D I	1.357	0.126
A E G	6.877	1.821	B E G	7.354	2.547	C E G	5.901	0.936
A E H	8.314	3.287	B E H	6.868	1.665	C E H	6.423	1.786
A E J	0.609	0.077	B E I	0.368	0.060	C E I	0.567	0.061
A F G	5.103	2.275	B F G	8.167	2.935	C F G	7.344	1.330
A F H	7.326	3.231	B F H	9.242	3.520	C F H	7.158	1.356
A F I	0.758	0.027	B F I	0.977	0.154	C F I	1.049	0.071

Mean value and standard deviation for sample families used in fatigue tests (all dimensions in μm)

Fig. 4 σ–ε graph for a vertically built sample
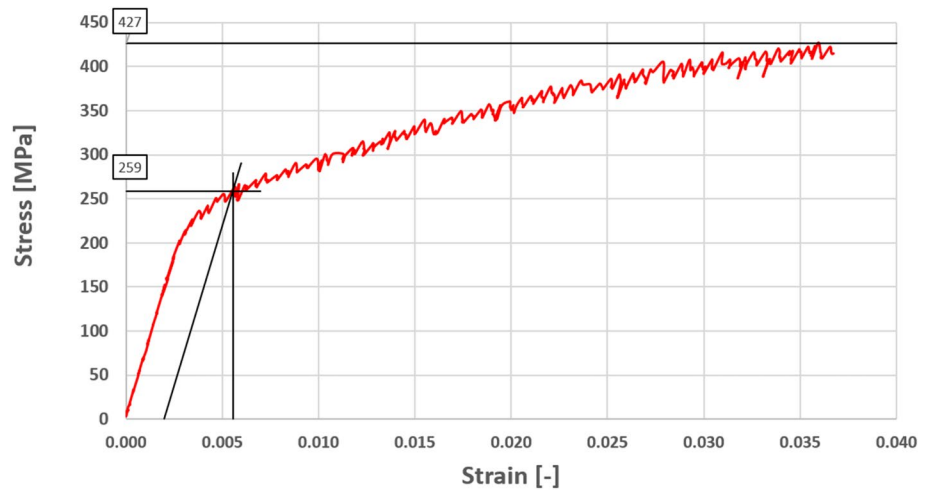
in the EOS datasheet that was available as of 2019 [52]. This datasheet has been regarded as a valid reference, considering that Young's modulus values are not available in the last published one [42]. The static strengths reported in [42, 52] are also consistent apart from a few minor differences. Differences due to the build orientations, affecting the yield strengths and elastic modulus, are not significant (analyses of variance with subsequent Fisher Tests were carried out on the $Rp_{0.2}$ and E results for this purpose).

Conversely, unexpected results were found for the ultimate tensile strengths (UTS). Lower values, even by 20%, were observed (Fig. 6). Furthermore, the ultimate tensile strength was found to be significantly affected by the build orientation. Regarding this point, a higher UTS was found for vertically oriented samples rather than for horizontally built ones. Cracks and consequent failures were observed in correspondence of the supported regions. Thus, defects induced by support detachment and geometrical errors (see analyses below on fatigue samples), with reference to horizontally fabricated samples, are likely to have led to lower ultimate strengths than those declared by the supplier.

3.3 Fatigue tests results

As for fatigue tests, the results were processed by the linear model according to Eqs. (4) and (5). Complying with the recommendations in [ISO 12107], the general linear test (GLT) was applied to assess if the improvements yielded by the adoption of a higher-order model were significant. A Fisher test proved that a quadratic model could provide just a negligible improvement, and this outcome was the same for all the datasets; therefore, a linear model was applied for all of them.

$$\mathrm{Log}(N) = b_0 + b_1 \cdot \mathrm{Log}(S), \tag{4}$$

$$S = 10^{\frac{b_0}{b_1}} \cdot N^{-\frac{1}{b_1}}. \tag{5}$$
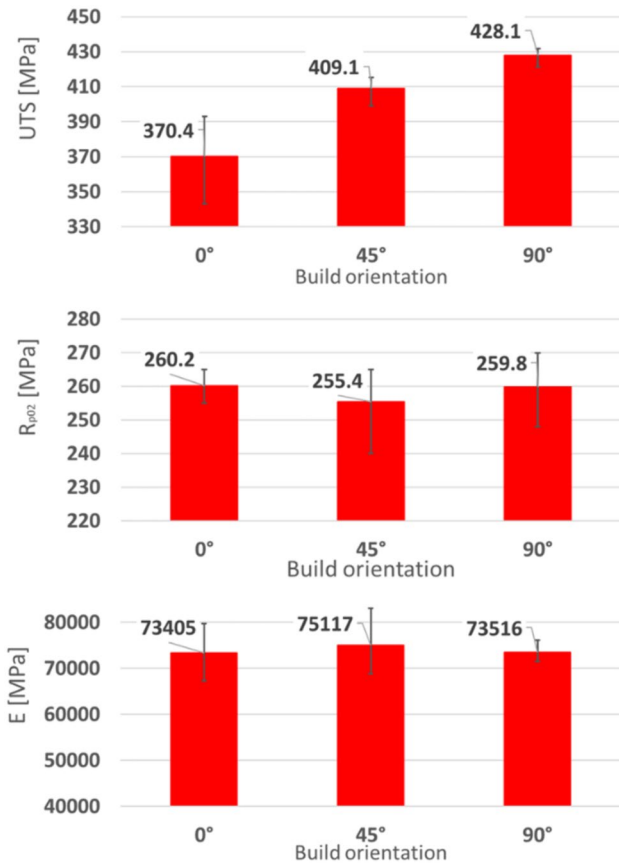
The analyzed S–N curves are discussed in the next section.

Fig. 5 Experimental results of static tensile tests

3.4 Density tests results

The density measurement results are resumed in Fig. 7 in terms of set grand mean. No significant differences were found among the sets. For comparison, the data sheet density is also indicated by a red dotted line.

3.5 Geometrical errors

A particular issue occurred for horizontally built samples, which compromised the results of some fatigue tests. Before the tests, two types of geometric errors affecting the ADG, ADH, AEG, and AEH sets were found. The first one is a circularity error: specimens exhibited an oval section with a measurement difference between two orthogonal diameters up to 0.4 mm. The second error was related to misalignment upon rotation: Table 6 shows the average values and maximum values found in the mentioned sets.

Horizontally built samples require supports at the gage diameter. After their removal, residual stress is usually released: in this case, this led to specimens' significant bending. Furthermore, if the removal operation is not carefully carried out, the external surface may get damaged by the excessive material removal. As a consequence, the gage diameter is smaller than expected, and the cross section is made oval.

The non-circularity of most of the horizontally manufactured specimens (Axx sets) is shown in Fig. 8.

As highlighted in the pictures, the actual specimen profile was far away from the theoretical circular one. The fracture surfaces are oriented with the crack initiation
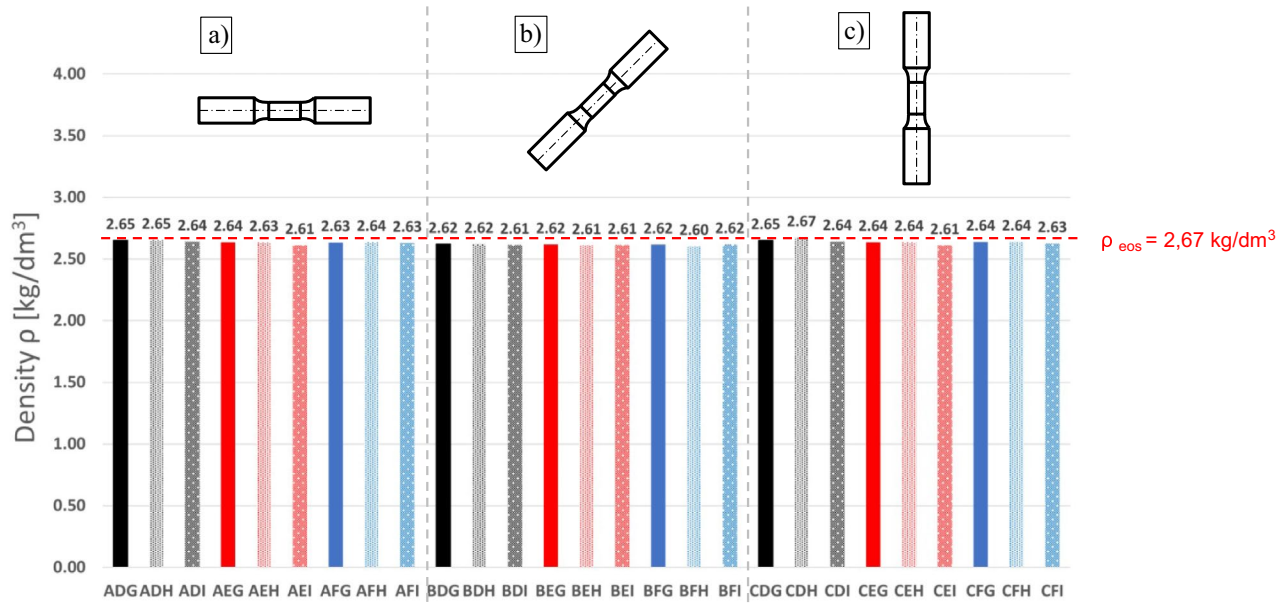
Fig. 6 Experimental static properties compared with those given by the powder datasheet [52]

Experimental

UTS [MPa]		mean	st.dev
BUILD ORIENTATION	0°	370.4	19.9
	45°	409.1	6.1
	90°	428.1	4.4
Rp$_{02}$ [MPa]		mean	st.dev
BUILD ORIENTATION	0°	260.2	4.3
	45°	255.4	9.7
	90°	259.8	9.3
E [MPa]		mean	st.dev
BUILD ORIENTATION	0°	73405	5369
	45°	75117	5299
	90°	73516	1846

EOS datasheet

Mechanical properties of the parts

	As built
Tensile strength [6]	
– in horizontal direction (XY)	460 ± 20 MPa / 66.7 ± 2.9 ksi
– in vertical direction (Z)	460 ± 20 MPa / 66.7 ± 2.9 ksi
Yield strength (Rp 0.2 %) [6]	
– in horizontal direction (XY)	270 ± 10 MPa / 39.2 ± 1.5 ksi
– in vertical direction (Z)	240 ± 10 MPa / 34.8 ± 1.5 ksi
Modulus of elasticity	
– in horizontal direction (XY)	75 ± 10 GPa / 10.9 ± 0.7 Msi
– in vertical direction (Z)	70 ± 10 GPa / 10.2 ± 0.7 Msi

[6] Mechanical strength tested as per ISO 6892–1:2009 (B) annex D, proportional specimens, specimen diameter 5 mm, original gauge length 25 mm (1 inch).

Fig. 7 Density measurements for all the studied sample sets

Table 6 Misalignment errors in horizontally built samples

Set	Mean misalignment (mm)	Maximum measured value (mm)
A D G	2.13	2.65
A D H	4.42	5.10
A E G	1.91	2.90
A E H	2.34	3.75

area in the upward position. Moreover, in these sets, the upper part of the image corresponds to the area where supports were removed. An irregular geometry is likely to have led to an irregular stress distribution, and surface defects acted as crack triggers. Furthermore, if the geometry is significantly damaged, the gravity center of the sample shifts from the longitudinal axis, thus inducing

vibrations during fatigue tests. Consequently, results have indeed been affected by these geometrical errors, which led to a worsening of the fatigue performance. Similar irregular shapes were also observed for ADG, ADH, AEG, and AEH sets, which actually proved to have a fatigue performance being far less than expected. Although AFG and AFH sets were manufactured with the same orientation and surface finishing, a regular shape was also found for them. This outcome indicates that the geometric errors were due to a careless removal of the supports, which occurred only for some specific sample sets. All the specimens involved in this experiment were manufactured by an external company, making it impossible to control the production phases. Furthermore, the samples were delivered in different batches, which could mean that supports were removed by different operators. A regular shape was found in samples with slanted

Fig. 8 Stereoscopic images of fracture surfaces in horizontally built samples for shot-peened (ADG01) and shot-peened and fine-blasted (AEH04) surface finishing
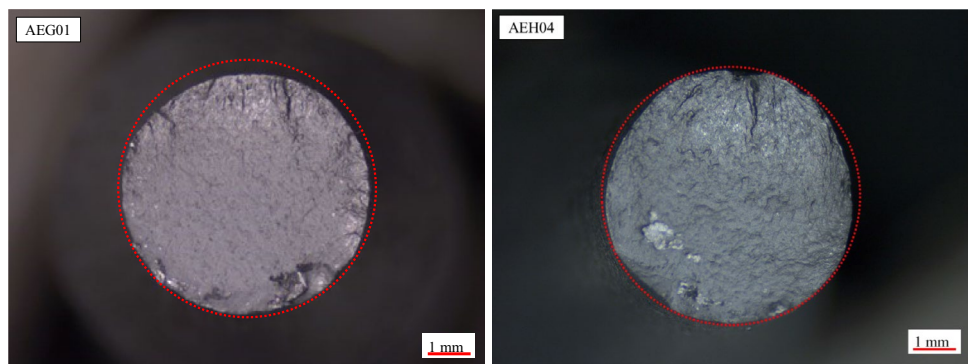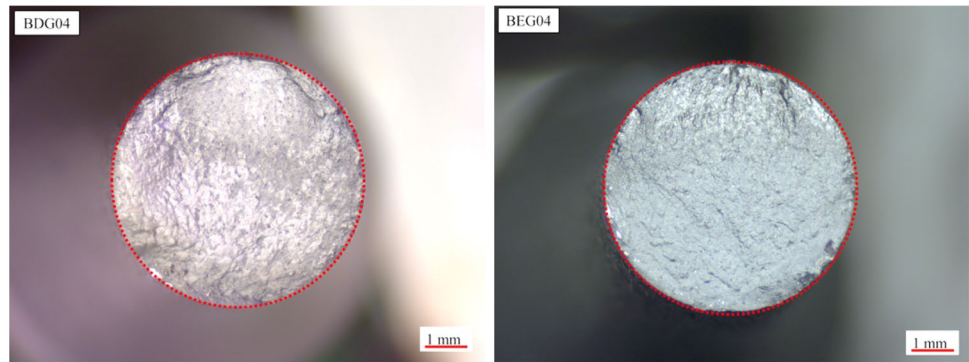
Fig. 9 Stereoscopic images of fracture surfaces in slanted built and shot-peened samples

orientation, as shown in Fig. 9. In machined samples, no geometrical errors were found for either horizontal or slanted orientations.

A section with remarkable circularity errors was also highlighted by stereoscopic microscope (Fig. 10a) observations. The optical microscope was then used to take pictures at higher magnification. Figure 10b shows the last manufactured layer, where melting pools, which are found to have 245 mm depth, are clearly visible. Figure 10c shows many porosities in the areas close to the supports. Geometric non-uniformities combined with high porosity caused stress intensification that led to premature fatigue failure.

These results indicate that, when fabricating parts lying horizontally on the build plane, support shaping and removal are critical issues that may significantly affect the mechanical performance.

4 Discussion

4.1 Statistical assessment

An ANOVA-based extended statistical method was adopted to properly compare the S–N curves. This method was successfully adopted for two-factor experiments [19, 53–55] and was here upgraded for this three-factor design in order to assess whether the differences among the curves are significant when compared to the observed scatter affecting the interpolated data. The curve trends were compared, averaging their differences over the lifespan ranging from 10^3 to 10^6 cycles, which corresponds to the observed lifespan.

The first step of the analysis is the computation of the gran mean curve S, as reported in Eq. (6).

$$\overline{S} = \frac{\sum_{i=A}^{C} \sum_{j=D}^{F} \sum_{k=G}^{I} S_{ijk}}{n_{\text{tot}}}, \tag{6}$$

Fig. 10 Cross section in a horizontally as-built sample observed by a stereoscope (**a**). Details of the melting pools (**b**) and the supported area (**c**) captured by the optical microscope
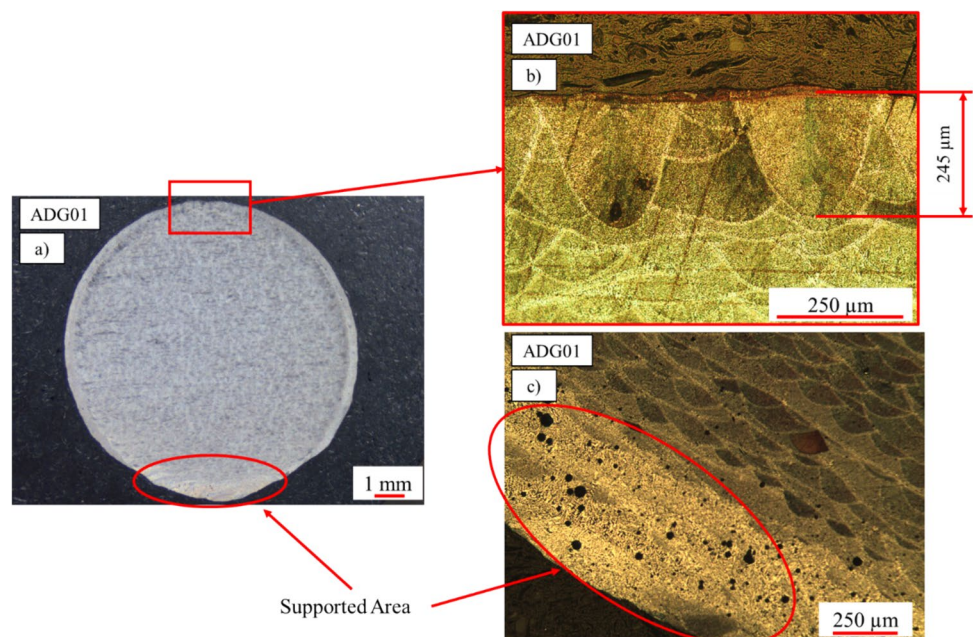
where S_{ijk} indicates the 10-base logarithm of the stress corresponding to generic fatigue life, whereas the subscript corresponds to the previously described sample families. The usual symbol for summations was used here, but with reference to the alphabet letters: thus, "i" can vary between A, B and C; "j" can vary between D, E and F; "k" varies between G, H and I (Fig. 11). n_{tot} represents the overall number of combinations between the factors, in this case, 27. The summation is the sum of all the fatigue curves of the 27 families. The second step of the analysis consists in the computation of the row mean ($S_{i..}$), the column mean ($S_{.j.}$), and the profundity mean ($S_{..k}$), where the symbol "$i_{..}$" in "$S_{i..}$" refers to the i-th row, all the columns and all the depths. Similar meanings have $S_{.j.}$ and $S_{..k}$. The n_p term symbolizes the number of families considered for the evaluation of the mean terms. In this experiment, it is the same for all the three considered factors, and it is equal to 9.

$$S_{i..} = \frac{\sum_{y=D}^{F} \sum_{z=G}^{I} S_{iyz}}{n_p}, \tag{7}$$

$$S_{.j.} = \frac{\sum_{x=A}^{C} \sum_{z=G}^{I} S_{xjz}}{n_p}, \tag{8}$$

$$S_{..k} = \frac{\sum_{x=A}^{C} \sum_{j=D}^{F} S_{xjk}}{n_p}. \tag{9}$$

To evaluate the effect of each factor, it is necessary to calculate the three terms SSBR (sum of square between rows, Eq. 10), SSBC (sum of square between columns, Eq. 11),

and SSBP (sum of square between profundities, Eq. 12), therefore considering the three different factors: build orientation (rows), heat treatments (columns), and surface treatments (profundities), respectively.

$$SSBR = n_p \cdot \sum_{i=A}^{C} \left(S_{i..} - \overline{S} \right)^2, \tag{10}$$

$$SSBC = n_p \cdot \sum_{j=D}^{F} \left(S_{.j.} - \overline{S} \right)^2, \tag{11}$$

$$SSBP = n_p \cdot \sum_{k=G}^{I} (S_{..k} - \overline{S})^2. \tag{12}$$

The last sets of terms needed are related to the interaction between the three factors (SSI, Sum of Square Interaction):

$$SSI = \sum_{i=A}^{C} \sum_{j=D}^{F} \sum_{k=G}^{I} (S_{ijk} - S_{ij.} - S_{i.k} - S_{.jk} + S_{i..} + S_{.j.} + S_{..k} - \overline{S})^2, \tag{13}$$

where

$$S_{ij.} = \frac{\sum_{k=G}^{I} S_{ijk}}{n_1}, \tag{14}$$

$$S_{i.k} = \frac{\sum_{J=D}^{F} S_{ijk}}{n_1}, \tag{15}$$

$$S_{.jk} = \frac{\sum_{i=A}^{C} S_{ijk}}{n_1}. \tag{16}$$

The number of families considered for the mean computation n_1 was 3. The interactions between pairs of factors were also taken into account through the terms:

$$SSI(RC) = n_1 \cdot \sum_{i=A}^{C} \sum_{j=D}^{F} \left(S_{ij.} - S_{i..} - S_{.j.} + \overline{S} \right)^2, \tag{17}$$

$$SSI(CP) = n_1 \cdot \sum_{j=D}^{F} \sum_{k=G}^{I} \left(S_{.jk} - S_{.j.} - S_{..k} + \overline{S} \right)^2, \tag{18}$$

$$SSI(RP) = n_1 \cdot \sum_{i=A}^{C} \sum_{k=G}^{I} \left(S_{i.k} - S_{i..} - S_{..k} + \overline{S} \right)^2. \tag{19}$$

The aforementioned terms were computed over the entire lifespan with a sufficiently refined step using an Excel sheet. Afterward, they were turned into scalars, taking the respective integral means over the entire life range
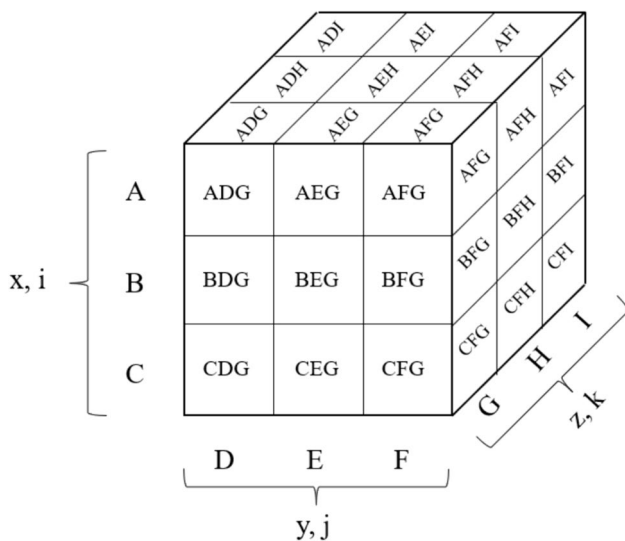

Fig. 11 Representation of the 3^3 experimental plan

to have reliable global indicators of the average impact of main factors and related interactions over the investigated life domain. The last term to be computed was the error-related term SSE. It can be regarded as the sum of the squares of the residuals between the experimental data distributions and the retrieved S–N curves. This term may be estimated based on Eq. 20, where S_{exp} represents the logarithm of the stress level corresponding to an observed life and S_{calc} indicates the same stress level in the logarithm scale, based on the interpolated S–N curve for the same life extent (based on Eq. 4). In this formula, the subscripts "i", "j", and "k" retain the same meanings as above, indicating the row, the column and the profundity of the experimental design in Fig. 11, whereas "l" identifies the l-th experimental point and n_{ijk} is the number of available points for the family i, j, k.

$$SSE = \sum_{i=A}^{C} \sum_{j=D}^{F} \sum_{k=G}^{I} \sum_{l=1}^{n_{i,j,k}} \left(S_{exp_{i,j,k,l}} - S_{calc_{i,j,k,l}} \right)^2. \tag{20}$$

A final step was needed to make the determined yields comparable to one another and to process them in a conventional two-factor ANOVA: the aforementioned terms were scaled, rationalizing them by the related degree of freedom. The outcome of the statistical assessment is reported in Table 7. Results highlight the significant effect of all the factors (with a 95% confidence level). Furthermore, all the interaction terms were found to be significant.

Despite the complex procedure, the results of the 3-way ANOVA analysis did not allow to derive detailed conclusions, as all the factors proved to be significant. However, it was a needed preliminary step before further processing. Afterward, the analyses were focused on smaller groups of tests in order to investigate the most significant effects and the most beneficial treatments in some specific conditions with design applications. Due to the observed geometrical criticalities, the aforementioned sample sets were excluded from further processing.

4.2 Influence of the parameters on the fatigue life

To exclude the geometrical errors found in the horizontally built samples, machined samples only were considered first to assess the effects of build orientation and heat treatment. Figure 12 shows the S–N curves for machined samples. Colors refer to the heat treatment (black for as-built, red for T6 heat treatment, light blue for stress relief), whereas the type of line refers to the build orientation (continuous lines for horizontally built samples, dashed lines for slanted built samples, dotted line for vertically built samples). Table 8 is the related ANOVA table that was determined following the rules of a two-factor (3^2) experiment to be regarded as a subset of the previously described 3^3 campaign. The heat treatment significantly affects the fatigue curves (high and significant SSBR term). Particularly, a detrimental contribution of the stress relief treatment is highlighted in Fig. 12. Conversely, the T6 heat treatment seems to ensure better fatigue properties.

On the other hand, build orientation does not significantly affect the fatigue properties.

Another comparison was carried out among the samples that had undergone T6, which appears to ensure the best fatigue performance, with the aim of highlighting the effects of build orientation and surface finishing. The curves and the results of the ANOVA analysis are listed in Fig. 13 and Table 9.

Due to the mentioned geometrical errors, which were likely to alter the results, only machined and heat-treated horizontally built samples were considered (AEI set) together with slanted and vertically built specimens. The surface finishing was considered as a row factor: the SSBR term highlights a significant influence of the surface treatment on the fatigue response of the AlSi10Mg heat treated. However, this influence turns out to be not significant at the 1% significance level and appears to be controversial when comparing the curves. At high cycles, the best fatigue performance was achieved for shot-peened and, shot-peened and fine-blasted samples. At low cycles, conversely, machining leads to higher fatigue life. Based on the ANOVA analysis,

Table 7 ANOVA results of the 3^3 experimental plan: SSBR refers to the build orientation, SSBC refers to the heat treatment, SSBP refers to the surface treatment

	SSQ	DoF	MSQ	Fcalc	p value	Significant?
SSBR	0.3757	2	0.1878	19.85	1.42E−08	YES
SSBC	0.8447	2	0.4223	44.64	1.09E−16	YES
SSBP	0.3275	2	0.1637	17.31	1.21E−07	YES
SSI(RC)	0.1433	4	0.0358	3.78	5.47E−03	YES
SSI(RP)	0.2589	4	0.0647	6.84	3.57E−05	YES
SSI(CP)	0.1556	4	0.0389	4.11	3.20E−03	YES
SSI	0.1975	8	0.0247	2.61	9.84E−03	YES
Error	1.8451	195	0.0095			
Total	4.1483	221				

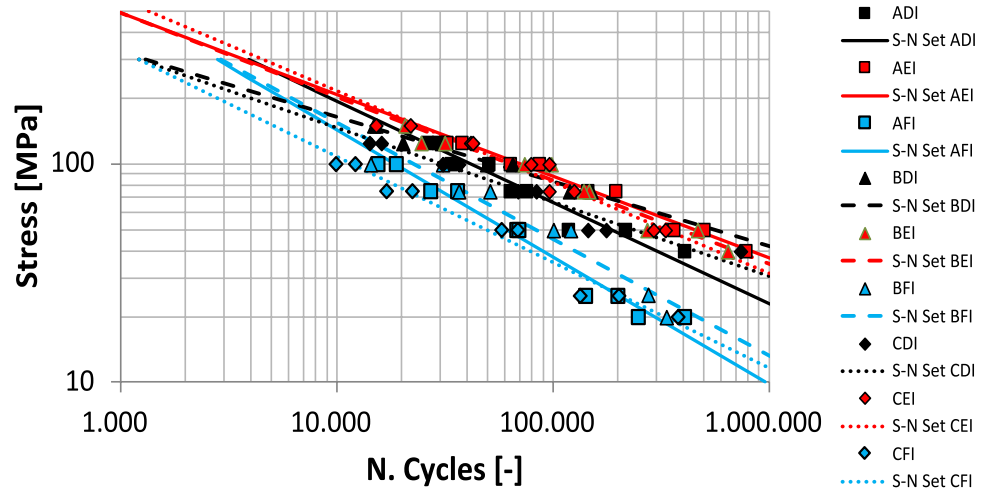**Fig. 12** Stress amplitude–N curves for machined samples

Table 8 ANOVA analysis for machined samples: SSBR refers to the heat treatment, SSBC refers to the build orientation and SSI refers to the interaction between the former parameters

	SSQ	DoF	MSQ	Fcalc	*p* value	Significant?
SSBR	0.2043	2	0.1021	43.84	5.16E−13	YES
SSBC	0.0107	2	0.0053	2.29	1.09E−01	NO
SSI	0.0090	4	0.0022	0.96	4.33E−01	NO
Error	0.1608	69	0.0023			
Total	0.3847	77				

Fig. 13 Stress amplitude–N curves for heat-treated samples
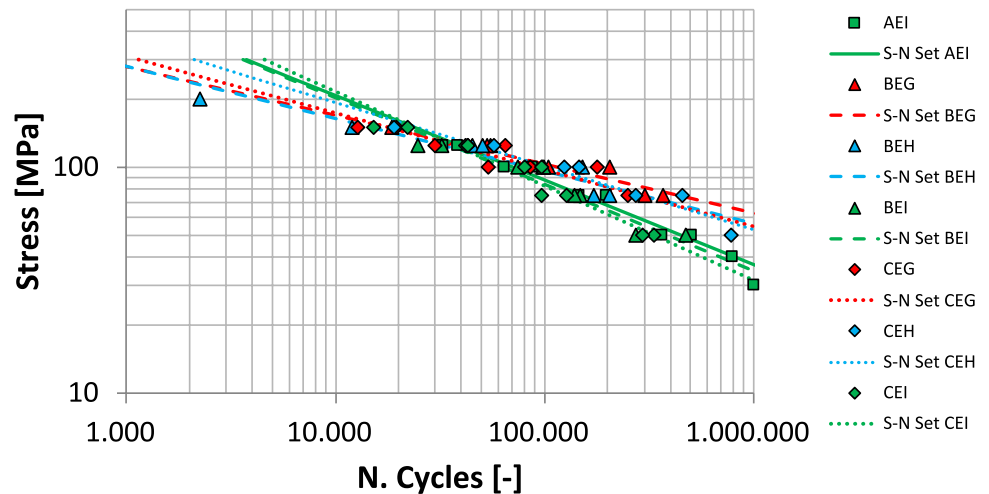
build orientation does not significantly affect the results. As highlighted in Fig. 13, curves of the same surface treatment are partially overlapped. These outcomes indicate that using machined and/or T6-treated samples steers a uniform fatigue behavior.

4.3 Fracture surface analysis

Fracture surface analysis showed that for not machined specimens, fracture initiated from the surface and was promoted by surface roughness and defects. For horizontally built specimens (Axx sets), the initiating point was found to be mostly located in the neighborhood of the areas where supports had been applied. Regarding slanted specimens (Bxx sets), cracks were found to mostly initiate in the gage area, on the side facing down during manufacturing. This occurrence is probably due to the higher roughness at this side of specimens if compared to that at the upper face. In turn, this was due to the stacking process, considering that no supports were acting under the gage upon slanted sample

Table 9 ANOVA analysis for T6 heat-treated samples: SSBR refers to the surface treatment, SSBC refers to the build orientation

	SSQ	DoF	MSQ	Fcalc	*p* value	Significant?
SSBR	0.0189	2	0.0095	4.88	1.23E−02	YES
SSBC	0.0008	1	0.0008	0.42	5.22E−01	NO
SSI	0.0006	2	0.0003	0.15	8.65E−01	NO
Error	0.0833	43	0.0019			
Total	0.1035	48				

fabrication. As for machined samples (xxI sets), the initiating points were located at both surface defects and subsurface porosities, regardless of build orientation. Different crack initiation sources observed by SEM-FEG are shown in Figs. 14, 15, and 16.

The actual hatch spacing was found to range from 150 to 180 μm. This value is likely to affect the number and the dimensions of porosities and defects that, in turn, have an influence on the fatigue life: in [41, 48], where the hatch spacing is greater, up to 220 μm, a lower fatigue strength was found. Thus, the measured value in the present study is in a range that should ensure good fatigue behavior. The contour thickness was found to be equal to 250 μm, aligned with the values from the literature.

4.4 Heat treatment strengthening effect

The effect of the heat treatment on the microstructure is visible in Fig. 17 and Fig. 18. From both stereoscopic and optical microscope observations, no differences between the as-built condition and the stress relief condition were found: in these cases, the microstructure is composed by α-Al columnar grains and a fibrous Si network (Fig. 17a and c).

This type of microstructure is a consequence of the fast cooling rate that is experienced during the process, as also confirmed by literature [23, 45, 56]. Moreover,

the optical microscope micrographies highlight a smaller grain size within the scan and a larger one in the overlap area between two adjacent hatches (Fig. 18b and f).

T6 heat-treated specimens showed a radically different microstructure instead. Stereoscopic images highlight a homogeneous section with not easily distinguishable laser scans (Fig. 18c). A microstructure that remains the same regardless of the build orientation was revealed by the optical microscope Fig. 18d). High-magnification SEM-FEG images (Fig. 17b) highlight that after age hardening, Si appears to be concentrated in particles (light gray in the picture, mean width of 3 μm). Thus, the different microstructure can be regarded as the primary reason for the better fatigue strength of the samples treated by T6. On the other hand, the same analysis confirms that stress relief is ineffective, as microstructure is left unchanged with respect to untreated parts.

As for the chemical composition of the considered area, the analyses was conducted through the same SEM equipment, by using the images of a very limited area and averaging the results over the same area (10 μm x 10 μm). The analysis highlighted a higher concentration of Silicon than that declared by the powder supplier (15.9% average against the expected 9–11%; see Table 10). However, it must be highlighted that this type of result refers to a

Fig. 14 Crack initiation source due to superficial and sub-superficial defects (sample AEG05, horizontally built, T6 heat treated and micro-shot-peened)
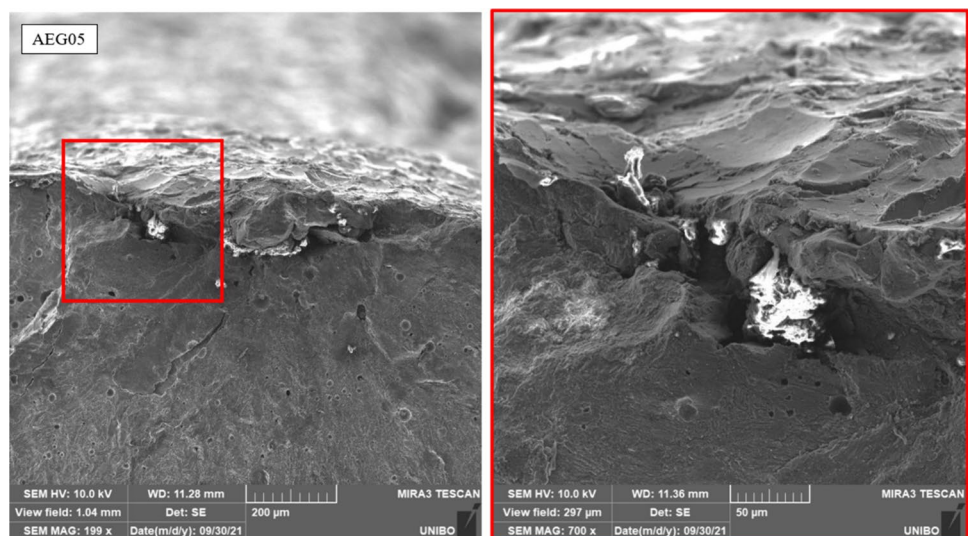
Fig. 15 Crack initiating source from a superficial defect (sample BEG05, slanted built, T6 heat treated, micro-shot-peened)
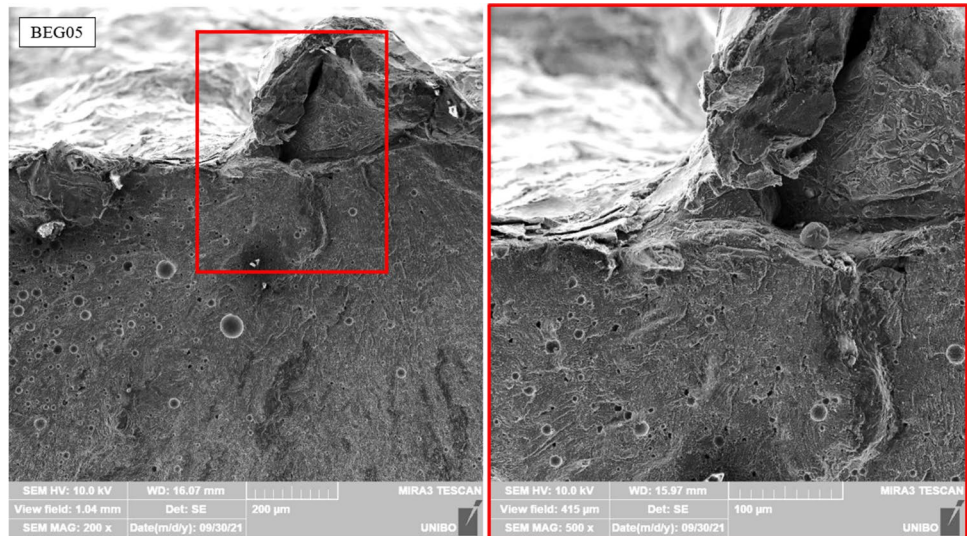
Fig. 16 Crack initiation source from superficial imperfection and a detail of unmelted powder (sample ADG10, horizontally built, T6 heat treated and micro-shot-peened)
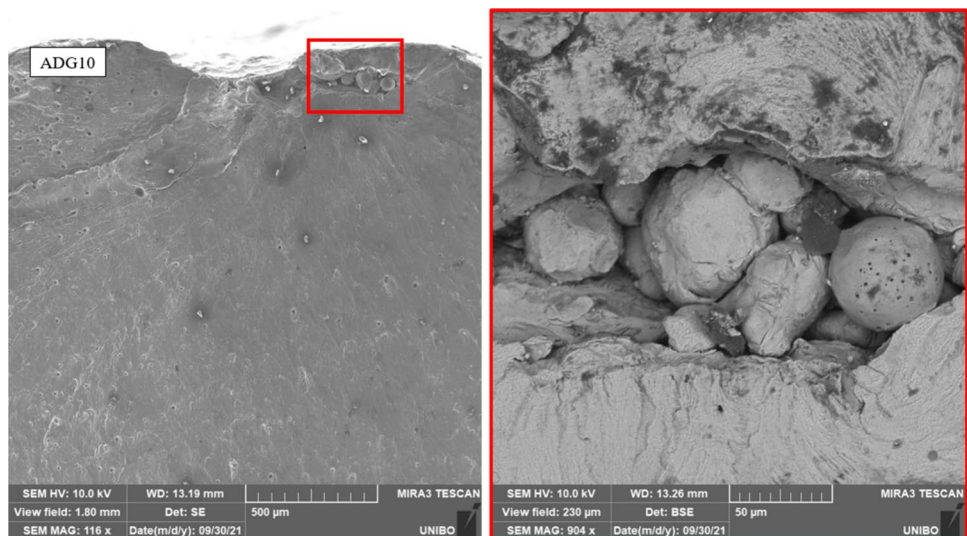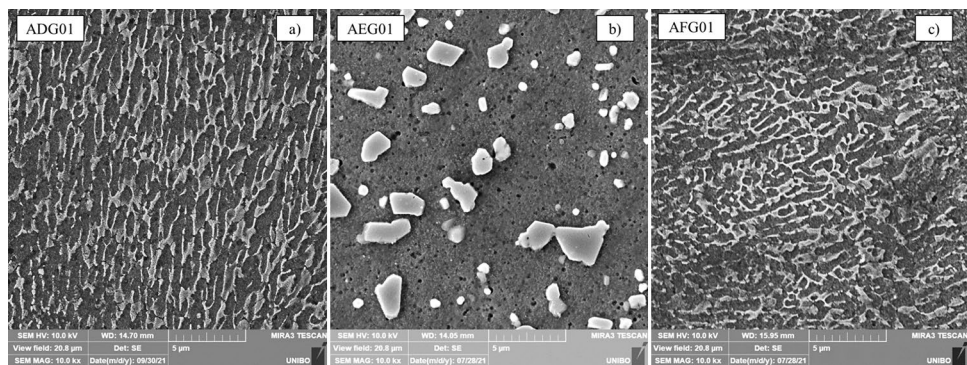
Fig. 17 High magnification SEM-FEG images. Microstructure in as-built samples (**a**), after T6 heat treatment (**b**), after stress relief (**c**)

portion of the samples and cannot be representative of the chemical composition of the entire sample.

4.5 Fracture behavior

A last stage of SEM-FEG analysis was carried out to accurately investigate the fracture behavior of the specimens

Fig. 18 Stereoscopic images (**a**, **c**, **e**) and optical microscopic images (**b**, **d**, **f**) of chemically etched surfaces for samples as built (**a**, **b**), T6 heat-treated (**c**, **d**) and stress relieved (**e**, **f**)
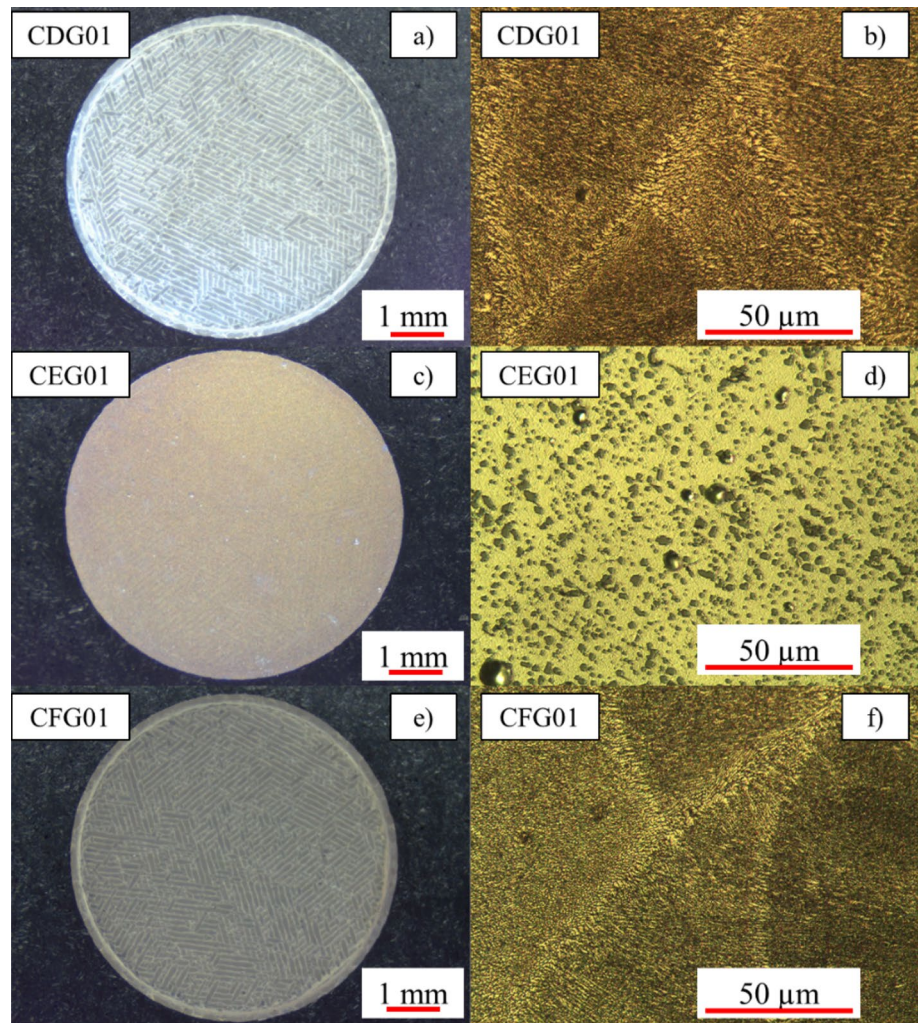
Table 10 Chemical compounds for the analyzed sets

	Al	si	Fe	Cu	Mn	Mg	Ni	Zn	Pb	Sn	Ti
ref	Ba	9–11	0.55	0.05	0.45	0.25–0.45	0.05	0.1	0.05	0.05	0.15
ADG	86.70	15.00	0.26	0.02	0	0.14	0.01	0	0.04	0.05	0
AEG	80.10	17.24	0.08	0.64	0	0.8	0.43	0.55	0.05	0	0.11
AFG	84.12	15.52	0.15	0	0.03	0.15	0	0	0	0	0.03

(Fig. 19) as an effect of different heat treatments.

As-built specimens (xDx sets) and stress-relieved specimens (xFx sets) display a mixed (ductile and brittle) fracture behavior, as dimples and cleavage facets are not clearly visible, whereas T6 heat-treated specimens (xEx sets) highlight a high amount of dimples (Fig. 20) on the final fracture zone (OFZ), which indicates a completely ductile fracture behavior following this treatment.

5 Conclusions

In this study, the fatigue performance of additively manufactured AlSi10Mg aluminum alloy was evaluated, determining the effects of building orientation, heat treatment and surface treatment. All the considered factors were found to affect fatigue strength. However, the effect of
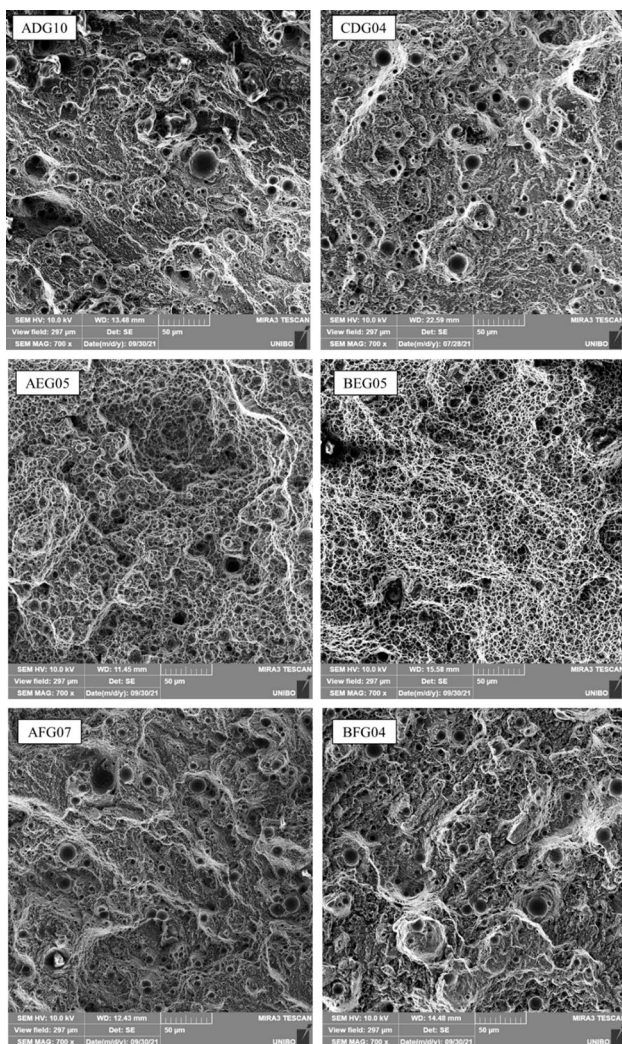
Fig. 19 High-magnification SEM images of the overload fracture zone (OFZ) for specimens in the as-built condition (samples with IDs ADG10 and CDG04), T6 heat-treated samples (IDs AEG05 and BEG05), and stress-relieved samples (IDs AFG07 and BFG04)

Fig. 20 Particular of the overload fracture zone (OFZ) for T6 heat-treated samples (AEG05), with clearly visible dimples

each one is affected by the level of the other two (which indicates a high interaction between the factors).

Regarding the heat treatments, it has been highlighted that the stress relief treatment did not lead to improvements, and it even led to worse fatigue strength in many cases.

The T6 heat treatment had a remarkably positive effect on fatigue life, which arises from an increase in ductility (supported by the SEM analyses that have been conducted) and complete microstructure enhancement as a result of the generation of uniform size Si particles. No differences in terms of fatigue strength were found for all the considered build orientations in T6 heat-treated samples, meaning that it was significantly beneficial regardless of the part build orientation.
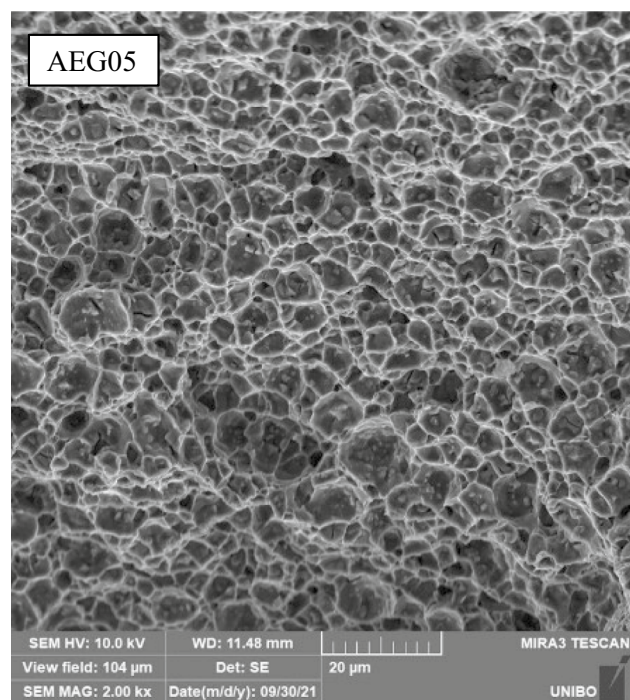
Regarding surface treatments, machining was found to be the least performing in terms of fatigue life at a high number of cycles. The best results were obtained for shot-peened families. In fact, residual compressive stresses, which are beneficial from the point of view of fatigue strength, are induced in the specimen's outer layer. Conversely, following machining, the outer layers are removed, thus eliminating the beneficial effect of shot-peening.

On the other hand, machining allows the removal of the defects located on the outer layers, mainly at the interface between contours and internal scans, which improves strength under high loads and for reduced lifespan. In fact, the fatigue response differences between the machined series were very small and appeared to be essentially dependent on the carried-out heat treatment and independent of the build orientation. Furthermore, machined specimens led to less scattered fatigue data.

Finally, the highest fatigue limit was observed for slanted, T6 heat-treated and shot-peened samples (BEG series). However, also in this case, the observed fatigue strength was under expectations. The calculated fatigue limit (in terms of stress amplitude) at 10^6 cycles was 62.8 MPa, whereas the supplier provided a limit of 110 MPa at $2 \cdot 10^7$ cycles for machined and non-heat-treated specimens [42].

Static tensile tests also highlighted lower performance than that declared by the powder supplier: the achieved yield strength and elastic modulus were aligned with those

expected, whereas the ultimate tensile strength was even 20% lower than the declared.

The analysis of the alloy compound showed a Silicon percentage outside the imposed limits (15% against a range of 9–11%), which could further explain the performance differences.

Declarations

References

1. Ngo TD, Kashani A, Imbalzano G, Nguyen KTQ, Hui D (2018) Additive manufacturing (3D printing): a review of materials, methods, applications and challenges. Compos Part B Eng 143:172–196. https://doi.org/10.1016/j.compositesb.2018.02.012
2. Banadaki Y, Razaviarab N, Fekrmandi H, Sharifi S (2020) Toward enabling a reliable quality monitoring system for additive manufacturing process using deep convolutional neural networks, pp 1–8. http://arxiv.org/abs/2003.08749
3. Ilani MA, Banad YM (2024) Modeling melt pool geometry in metal additive manufacturing using Goldak's semi-ellipsoidal heat source: a data-driven computational approach. https://arxiv.org/abs/2404.08834v1
4. Abe F, Osakada K, Shiomi M, Uematsu K, Matsumoto M (2001) The manufacturing of hard tools from metallic powders by selective laser melting. J Mater Process Technol 111:210–213. https://doi.org/10.1016/S0924-0136(01)00522-2
5. Bourell DL, Beaman JJ, Leu MC, Rosen DW (2009) A Brief History of Additive manufacturing and the 2009 roadmap for additive manufacturing: looking back and looking ahead, US Turkey workshop on rapid technologies, Rapid Technol 5–11
6. Nicoletto G (2018) Directional and notch effects on the fatigue behavior of as-built DMLS Ti6Al4V. Int J Fatigue 106:124–131. https://doi.org/10.1016/J.IJFATIGUE.2017.10.004
7. Kruth J, Mercelis P, Van Vaerenbergh J, Froyen L, Rombouts M (2005) Binding mechanisms in selective laser sintering and selective laser melting. Rapid Prototyp J 11:26–36. https://doi.org/10.1108/13552540510573365
8. Aliakbari M (2012) Additive manufacturing: state-of-the-art, capabilities, and sample applications with cost analysis
9. Pandey PM (2010) Rapid prototyping technologies, applications and part deposition planning. Retr Oct 15:550–555
10. Herderick E (2011) Additive manufacturing of metals: a review, In: Materials science and technology conference exhibition, pp 1413–1425
11. Shellabear M, Nyrhilä O (2004) DMLS-Development history and state of the art, Laser Assist. Netshape Eng. 4, Proc. 4th LANE, pp 21–24
12. ISO/ASTM 52900:2021 (2021) Additive manufacturing: general principles—fundamentals and vocabulary
13. Delahaye Jocelyn MA, Habraken Anne M (2023) 2D FE modeling of the thermal history of the heat affected zone in AlSi10Mg LPBF, pp 189–198. https://doi.org/10.21741/9781644902479-21
14. Li Y, Gu D (2014) Thermal behavior during selective laser melting of commercially pure titanium powder: numerical simulation and experimental study. Addit Manuf 1:99–109
15. Brandl E, Heckenberger U, Holzinger V, Buchbinder D (2012) Additive manufactured AlSi10Mg samples using Selective Laser Melting (SLM): Microstructure, high cycle fatigue, and fracture behavior. Mater Des 34:159–169. https://doi.org/10.1016/j.matdes.2011.07.067
16. Yang T, Liu T, Liao W, MacDonald E, Wei H, Chen X, Jiang L (2019) The influence of process parameters on vertical surface roughness of the AlSi10Mg parts fabricated by selective laser melting. J Mater Process Technol 266:26–36
17. Sagbas B (2020) Post-processing effects on surface properties of direct metal laser sintered AlSi10Mg parts. Met Mater Int 26:143–153
18. Leuders S, Thöne M, Riemer A, Niendorf T, Tröster T, Richard HA, Maier HJ (2013) On the mechanical behaviour of titanium alloy TiAl6V4 manufactured by selective laser melting: fatigue resistance and crack growth performance. Int J Fatigue 48:300–307. https://doi.org/10.1016/j.ijfatigue.2012.11.011
19. Croccolo D, De Agostinis M, Fini S, Olmi G, Robusto F, Kostić SĆ, Vranić A, Bogojević N (2018) Fatigue response of as-built DMLS maraging steel and effects of aging, machining, and peening treatments. Metals. https://doi.org/10.3390/met8070505
20. Croccolo D, De Agostinis M, Fini S, Olmi G, Robusto F, Ciric-Kostic S, Vranic A, Muharemovic N, Bogojevic N (2019) Effects of machining and heat and surface treatments on as built DMLS processed maraging steel. Springer International Publishing. https://doi.org/10.1007/978-3-319-91989-8_24
21. Braun M, Mayer E, Kryukov I, Wolf C, Böhm S, Taghipour A, Wu RE, Ehlers S, Sheikhi S (2021) Fatigue strength of PBF-LB/M and wrought 316L stainless steel: effect of post-treatment and cyclic mean stress. Fatigue Fract Eng Mater Struct 44:3077–3093. https://doi.org/10.1111/ffe.13552
22. Gockel J, Sheridan L, Koerper B, Whip B (2019) The influence of additive manufacturing processing parameters on surface roughness and fatigue life. Int J Fatigue 124:380–388
23. Aboulkhair NT, Maskery I, Tuck C, Ashcroft I, Everitt NM (2016) The microstructure and mechanical properties of selectively laser melted AlSi10Mg: the effect of a conventional T6-like heat treatment. Mater Sci Eng A 667:139–146. https://doi.org/10.1016/j.msea.2016.04.092
24. Li W, Li S, Liu J, Zhang A, Zhou Y, Wei Q, Yan C, Shi Y (2016) Effect of heat treatment on AlSi10Mg alloy fabricated by selective laser melting: Microstructure evolution, mechanical properties and fracture mechanism. Mater Sci Eng A 663:116–125. https://doi.org/10.1016/j.msea.2016.03.088
25. Romano S, Nezhadfar PD, Shamsaei N, Seifi M, Beretta S (2020) High cycle fatigue behavior and life prediction for additively manufactured 17–4 PH stainless steel: effect of sub-surface porosity and surface roughness. Theor Appl Fract Mech. https://doi.org/10.1016/j.tafmec.2020.102477
26. Hackel L, Rankin JR, Rubenchik A, King WE, Matthews M (2018) Laser peening: A tool for additive manufacturing post-processing.

Addit Manuf 24:67–75. https://doi.org/10.1016/j.addma.2018.09.013

27. Aguado-Montero S, Navarro C, Vázquez J, Lasagni F, Slawik S, Domínguez J (2022) Fatigue behaviour of PBF additive manufactured TI6AL4V alloy after shot and laser peening. Int J Fatigue 154:106536. https://doi.org/10.1016/j.ijfatigue.2021.106536

28. de los Rios ER, Walley A, Milan MT, Hammersley G (1995) Fatigue crack initiation and propagation on shot-peened surfaces in A316 stainless steel. Int J Fatigue 17:493–499. https://doi.org/10.1016/0142-1123(95)00044-T

29. Zhu W, Ma C, Zhang C, Hu K, Zeng X (2023) Fatigue crack propagation behavior in Ti−6Al−4V alloy with surface gradient structure fabricated by high-energy shot peening. Trans Non-ferrous Met Soc China 33:3003–3016. https://doi.org/10.1016/S1003-6326(23)66313-7

30. Chen M, Deng W, Liu H, Wang R, Wang M, Duan Y, Jiang C, Ji V (2024) Enhancement of fatigue properties of selective laser melting fabricated TC4 alloy by multiple shot peening treatments. Int J Fatigue 182:108215. https://doi.org/10.1016/j.ijfatigue.2024.108215

31. Kumar P, Ramamurty U (2020) High cycle fatigue in selective laser melted Ti-6Al-4V. Acta Mater 194:305–320. https://doi.org/10.1016/j.actamat.2020.05.041

32. O'Brien JM, Montgomery S, Yaghi A, Afazov SM (2021) Process chain simulation of laser powder bed fusion including heat treatment and surface hardening. CIRP J Manuf Sci Technol 32:266–276. https://doi.org/10.1016/j.cirpj.2021.01.006

33. Kaynak Y, Kitay O (2019) The effect of post-processing operations on surface characteristics of 316L stainless steel produced by selective laser melting. Addit Manuf 26:84–93

34. Khan HM, Karabulut Y, Kitay O, Kaynak Y, Jawahir IS (2021) Influence of the post-processing operations on surface integrity of metal components produced by laser powder bed fusion additive manufacturing: a review. Mach Sci Technol 25:118–176. https://doi.org/10.1080/10910344.2020.1855649

35. Todai M, Nakano T, Liu T, Yasuda HY, Hagihara K, Cho K, Ueda M, Takeyama M (2017) Effect of building direction on the microstructure and tensile properties of Ti-48Al-2Cr-2Nb alloy additively manufactured by electron beam melting. Addit Manuf 13:61–70. https://doi.org/10.1016/j.addma.2016.11.001

36. Hitzler L, Janousch C, Schanz J, Merkel M, Heine B, Mack F, Hall W, Öchsner A (2017) Direction and location dependency of selective laser melted AlSi10Mg specimens. J Mater Process Technol 243:48–61

37. Kempen K, Thijs L, Van Humbeeck J, Kruth J-P (2012) Mechanical properties of AlSi10Mg produced by selective laser melting. Phys Procedia 39:439–446. https://doi.org/10.1016/j.phpro.2012.10.059

38. Rosenthal I, Shneck R, Stern A (2018) Heat treatment effect on the mechanical properties and fracture mechanism in AlSi10Mg fabricated by additive manufacturing selective laser melting process. Mater Sci Eng A 729:310–322. https://doi.org/10.1016/j.msea.2018.05.074

39. Maamoun AH, Xue YF, Elbestawi MA, Veldhuis SC (2019) The effect of selective laser melting process parameters on the microstructure and mechanical properties of Al6061 and AlSi10Mg alloys. Materials. https://doi.org/10.3390/ma12010012

40. Beevers E, Brandão AD, Gumpinger J, Gschweitl M, Seyfert C, Hofbauer P, Rohr T, Ghidini T (2018) Fatigue properties and material characteristics of additively manufactured AlSi10Mg–Effect of the contour parameter on the microstructure, density, residual stress, roughness and mechanical properties. Int J Fatigue 117:148–162

41. Tang M, Pistorius PC (2017) Oxides, porosity and fatigue performance of AlSi10Mg parts produced by selective laser melting. Int J Fatigue 94:192–201. https://doi.org/10.1016/j.ijfatigue.2016.06.002

42. EOS GmbH—Electro optical systems, material data sheet: EOS AlSi10Mg., (n.d.). https://www.eos.info/03_system-related-assets/material-related-contents/metal-materials-and-examples/metal-material-datasheet/aluminium/material_datasheet_eos_aluminium-alsi10mg_en_web.pdf

43. Bagherifard S, Beretta N, Monti S, Riccio M, Bandini M, Guagliano M (2018) On the fatigue strength enhancement of additive manufactured AlSi10Mg parts by mechanical and thermal post-processing. Mater Des 145:28–41. https://doi.org/10.1016/j.matdes.2018.02.055

44. Clement CD, Masson J, Kabir AS (2022) Effects of heat treatment on microstructure and mechanical properties of AlSi10Mg fabricated by selective laser melting process. J Manuf Mater Process. https://doi.org/10.3390/jmmp6030052

45. Amir B, Grinberg E, Gale Y, Sadot O, Samuha S (2021) Influences of platform heating and post-processing stress relief treatment on the mechanical properties and microstructure of selective-laser-melted AlSi10Mg alloys. Mater Sci Eng A 822:141612

46. Mfusi BJ, Mathe NR, Tshabalala LC, Popoola PAI (2019) The effect of stress relief on the mechanical and fatigue properties of additively manufactured AlSi10Mg parts. Metals 9:1–14. https://doi.org/10.3390/met9111216

47. BSI (2010) BS ISO 1143: 2010 BSI Standards Publication Metallic materials—rotating bar bending fatigue testing

48. Tang M, Pistorius PC (2019) Fatigue life prediction for AlSi10Mg components produced by selective laser melting. Int J Fatigue 125:479–490. https://doi.org/10.1016/j.ijfatigue.2019.04.015

49. Girelli L, Tocci M, Gelfi M, Pola A (2019) Study of heat treatment parameters for additively manufactured AlSi10Mg in comparison with corresponding cast alloy. Mater Sci Eng A 739:317–328

50. Girelli L, Tocci M, Montesano L, Gelfi M, Pola A (2017) Optimization of heat treatment parameters for additive manufacturing and gravity casting AlSi10Mg alloy. In: IOP conference series: materials science and engineering, IOP Publishing, p 12016

51. BSI (2016) BSI standards publication metallic materials—tensile testing Part 1: Method of test at room temperature (ISO 6892-1:2016), Bsi

52. EOS (2014) EOS aluminium AlSi10Mg material data sheet. GPI Prototype Manuf Serv 49:1–5

53. Croccolo D, De Agostinis M, Fini S, Olmi G, Bogojevic N, Ciric-Kostic S (2018) Effects of build orientation and thickness of allowance on the fatigue behaviour of 15–5 PH stainless steel manufactured by DMLS. Fatigue Fract Eng Mater Struct 41:900–916

54. Croccolo D, De Agostinis M, Fini S, Olmi G, Vranic A, Ciric-Kostic S (2016) Influence of the build orientation on the fatigue strength of EOS maraging steel produced by additive metal machine. Fatigue Fract Eng Mater Struct 39:637–647

55. Olmi G (2012) Low cycle fatigue experiments on turbogenerator steels and a new method for defining confidence bands. J Test Eval. https://doi.org/10.1520/JTE104548

56. Siddique S, Imran M, Wycisk E, Emmelmann C, Walther F (2015) Influence of process-induced microstructure and imperfections on mechanical properties of AlSi12 processed by selective laser melting. J Mater Process Technol 221:205–213. https://doi.org/10.1016/j.jmatprotec.2015.02.023